

Article

Geochemical Record of Late Quaternary Paleodepositional Environment from Lacustrine Sediments of Soda Lake, Carrizo Plain, California

Alejandro Rodriguez, Junhua Guo , Katie O'Sullivan and William Krugh

Department of Geological Sciences, California State University, Bakersfield, CA 93311, USA; arodriguez91@csub.edu (A.R.); kosullivan@csub.edu (K.O.); wkrugh@csub.edu (W.K.)

* Correspondence: jguo1@csub.edu

Abstract: This study investigates the responses of the depositional environments of Soda Lake sediments to climatic shifts from the Last Glacial Maximum to the Holocene epoch based on the results of major and trace elements of the North Soda Lake (NSL) NSL1A core. The NSL1A core records the sedimentary evolution of the Soda Lake watershed since at least 25 cal ka BP. Element analyses provide evidence that Soda Lake sediments are mostly derived from marine sequences in the Southern Coast Ranges of California. Variation in proxies for paleoweathering, paleoclimate, paleosalinity, paleoproductivity, paleoredox, and water depth is utilized to reconstruct the evolution of the sedimentary environment. The Chemical Index of Alteration (CIA) values indicate low to moderate chemical weathering in the sediment source regions. Paleoredox proxies indicate that the NSL1A core formed in a mainly subreduction environment. The NSL1A core is divided into four zones based on the results of the proxies. Zone 4 (5.0–5.8 m) of the sediment core indicates stable hydroclimatic conditions with low and constant sand and silt content, suggesting a warm and relatively humid environment. Zone 3 (3.35–5.0 m) represents the early half of the Last Glacial Maximum interval and a high lake stand. The elevated sand content suggests postflood events due to the northerly migration of westerly storm tracks. Zone 2 (1.075–3.35 m) reveals nuanced changes, including decreasing salinity, slight increases in wetness, detrital trace metals, and paleoproductivity. These subtle shifts suggest a multifaceted environmental evolution: a trend toward wetter conditions alongside a prolonged shift from cooler to warmer periods. Zone 1 (0.15–1.075 m) spans the Lateglacial to Holocene transition as well as Early and Middle Holocene, marked by significant hydrologic and ecologic variability including rapid warming during the Bølling–Allerød and rapid cooling linked to the Younger Dryas.

Keywords: Quaternary; lacustrine sediments; Carrizo Plain; paleoclimate; geochemistry; Last Glacial Maximum



Citation: Rodriguez, A.; Guo, J.; O'Sullivan, K.; Krugh, W. Geochemical Record of Late Quaternary Paleodepositional Environment from Lacustrine Sediments of Soda Lake, Carrizo Plain, California. *Minerals* **2024**, *14*, 211. <https://doi.org/10.3390/min14030211>

Academic Editors: Roberto Buccione and Rabah Kechiched

Received: 19 January 2024

Revised: 4 February 2024

Accepted: 16 February 2024

Published: 20 February 2024



Copyright: © 2024 by the authors. Licensee MDPI, Basel, Switzerland. This article is an open access article distributed under the terms and conditions of the Creative Commons Attribution (CC BY) license (<https://creativecommons.org/licenses/by/4.0/>).

1. Introduction

Southwest North America (SWNA), especially California, has recently experienced extended dry periods due to drought, leading to water management issues in the region. The ability to use climate models to predict changes in water resources in SWNA is crucial for aiding water management plans. Climate models, when not accounting for decadal variations caused by El Niño–Southern Oscillation events, generally agree that the SWNA hydroclimate will become increasingly drier as dry zones expand toward the poles [1,2]. Sedimentary records have been extensively utilized in paleoenvironmental reconstruction due to their ability to faithfully preserve original lithological features and document climatic fluctuations during deposition [3–6]. Changes in precipitation recorded in lake sediments can be used to assess climate models, such as those presented in the Intergovernmental Panel on Climate Change Assessment Report Four [1]. Thus, lakes around the SWNA region have been extensively investigated for paleoclimate research, including Owens

Lake, Tulare Lake, Baldwin Lake, Lake Elsinore, Dry Lake, Swamp Lake, Silver Lake, etc. (e.g., [7–35]).

However, few studies have been conducted on the Soda Lake sediments in the Carrizo Plain (Figure 1), despite its significance as it lies within a geographic gap in lake records associating high stands with the Last Glacial Maximum (LGM) [36]. Due to California's intricate geological and tectonic characteristics, climate records have revealed varying moisture patterns over time. For instance, sediment records from Swamp Lake in the central Sierra Nevada Mountains indicate reduced effective moisture levels and a higher incidence of wildfires, suggesting warm-summer conditions with intermittent dry periods during the Holocene [7–13]. In contrast, sediment records from the Holocene in Dry Lake [14–16], Lake Elsinore [17], San Joaquin Marsh [21], Tulare Lake [22,23], Owens Lake [24], and Silver Lake in the Great Basin [26] suggest a wetter Holocene. In summary, conducting an in-depth analysis of the sediments in Soda Lake is crucial for expanding the current understanding of paleoenvironmental changes in the SWNA region.

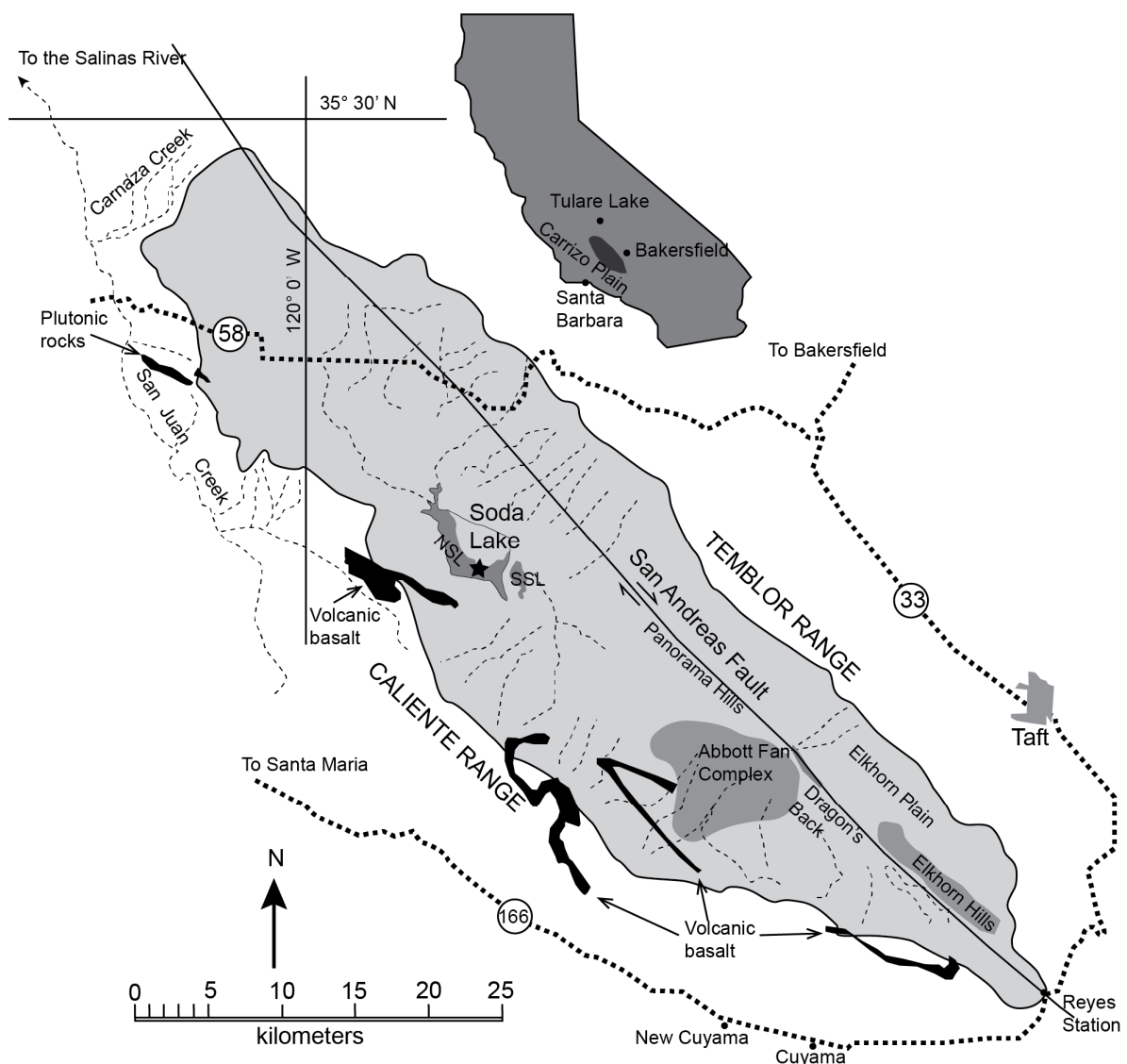


Figure 1. Location map showing the Carrizo Plain's drainage divide and the location of features referenced in the text and redrawn from [36]. The dashed line indicates the current drainage divide for the closed Carrizo Plain watershed, for which Soda Lake is the sink. The research area and core location map for North Soda Lake samples. NSL = North Soda Lake; SSL = South Soda Lake; star indicates the NSL1A core location.

Soda Lake is an ephemeral lake located in the Southern California Coast Ranges between the Temblor and Caliente Range in eastern San Luis Obispo County. It consists of a larger northern L-shaped basin and a smaller southern basin (Figure 1). In this tectonically closed system, sediments deposited over time provide an excellent archive for climate change studies. Unlike an open basin, sediments in a closed system avoid significant overprinting effects in the sedimentary record. Previous work on the lake has established relative lake levels based on sediment color, pollen assemblages, magnetic susceptibility, halite content, and the spectral gamma-ray data of North Soda Lake core samples [36,37]. Two previous lake high stands were revealed based on optically stimulated luminescence dates on clay dunes surrounding the current lake [36]. The upper 6 m of the NSL core correlate with the marine isotope stage (MIS) 2 pluvial event, responsible for pluvial lake high stands throughout the western United States [37]. Unlike freshwater lakes studied in the western United States, Soda Lake typically experiences more evaporation than freshwater influx evidenced by the diverse suite of chloride and sulfate minerals [37,38] and may have a more complicated interaction between the climatic environment and the depositional processes and salinity variations, as well as the lake levels.

This study aims to examine the chemical composition and variability in sediments from Soda Lake within the top 1 to 6 m of the Carrizo Plain. The two primary goals are (i) to elucidate the patterns of element distributions in these upper sediment layers and (ii) to reconstruct past climatic conditions, salinity levels, and redox environments in the Carrizo Plain. The results will offer valuable insights for future research on environmental changes in the late Quaternary period in the SWNA region.

2. Geologic Setting and Background

The Carrizo Plain, situated in the California Coast Range, is a tectonically closed basin bounded by the Temblor Range to the northeast and the Caliente Range to the southwest. It has a watershed that exceeds 1230 km² [38]. This basin is tectonically active, with a segment of the San Andreas Fault zone cutting through its eastern part, creating a notable contrast in lithologies due to a significant right lateral offset [39–41]. The basement complex west of the fault zone is comprised of Mesozoic granitic rocks intruding into older metamorphic rocks [40]. A Miocene sedimentary sequence overlies the basement complex. The oldest unit, the Simmler Formation, is nonmarine and is overlain by a marine sequence, reaching up to 14,000 ft in thickness in the Caliente Range and Carrizo Plain. On the eastern side of the fault zone, the oldest unit, the Franciscan Formation, primarily consists of lightly metamorphosed greywacke and serpentinite, overlain by a series of Neogene, Paleogene, and Cretaceous marine sedimentary sequences.

The section of the San Andreas Fault near the Carrizo Plain has been highly active since the deposition of the Paso Robles Formation during the Neogene period. Initially, drainage in the Carrizo Plain flowed southeast into the southern San Joaquin Valley until the region experienced uplift during the middle to late Pliocene [40,42]. This uplift marked the end of the Paso Robles Formation deposition and initiated a period of internal drainage in the Carrizo Plain [42]. In the late Pleistocene, due to southwestward tilting of the Gabilan Mesa and uplift in the Temblor Range, drainage in the plain reversed, causing water to flow out through the current northwest drainage point in the Carrizo Plain [42]. This reversal in drainage led to the formation of Soda Lake, a hydrologically closed basin, by the late Pleistocene. The closure of the northwest drainage point in the Carrizo Plain was caused by tilting in the valley, cutting off drainage and resulting in the formation of a tectonically closed basin in what was once the upper portion of the Salinas River Basin [36].

Soda Lake, now a playa and a closed depression in the Carrizo Plain, is a pluvial lake. The composition of sediments in such closed depressions is primarily influenced by groundwater chemistry, which varies with the openness of the basin. In hydrologically closed basins, the reaction between water and the underlying and surrounding lithologies is the main factor determining the primary solute composition [43]. Soda Lake is located in a hydrologically closed basin and is primarily fed by runoff. In this type of lake, if

evaporation exceeds the inflow of water, the lake will not be long-lasting, nor will it allow for significant accumulation of evaporite minerals [43]. Therefore, for a lake to become a perennial water body solely from repeated runoff events, the water table must eventually rise to produce a permanent lake. The rise in the water table occurs if precipitation exceeds evaporation. However, due to insufficient water volumes, Soda Lake cannot accumulate significant amounts of subaqueous evaporites.

3. Materials and Methods

3.1. Sample Collection and Lithology Characteristics

The samples used in this study were obtained from the NSL core drilled at (35°13'20" N, 119°52'50" W), near the southern end of the North Soda Lake pan (Figure 1) [36,37]. The NSL core consists of two drill sites with the core top at an elevation of ~584 masl (meters above sea level) on a portion of the former lake floor, NSL1A and NSL1B. Initial drilling of the lake sediments was obstructed at NSL1A, leading to its abandonment. Subsequently, drilling was carried out roughly two feet from the original location, and core collection began at a depth of 6 m below the ground surface. This second core site, NSL1B, has a total length of approximately 34 m. The total depth for the NSL core is approximately 40 m.

A physical core description was completed for the upper 18.5 mbgs (meters below ground surface) [36,37] to document composition, color, texture, grain size, and sedimentary structures. The core was found to be generally featureless and devoid of visible structures, except for some mottling in the upper core segments and rare lenses of gypsum crystals. It primarily consisted of fine-grained material and lacked sandy intervals. Variations in the core's color were documented using the Munsell color system.

The lithology of the core sediments consists of two end members (Figure 2) [36,37]. Throughout the majority of both cores, the sediments display oxidation. The oxidized sediment, characterized by a light olive-brown color (5Y 6/4), contains 1–10 mm euhedral bassanite ($\text{CaSO}_4 \cdot \frac{1}{2} \text{H}_2\text{O}$) crystals embedded in a clay matrix. Notably, distinct layering is infrequently observed. Two intervals with a reduced lithology are identified—one occurring midway down core NSL1 (17–20 m) and the other at the top of the cores (1–5 m). The reduced lithology is composed of dark-gray (5Y 4/1) or greenish-gray (10Y or 10GY 5/1) clays. Evaporite crystals are rare and occasionally appear in discrete layers. It is important to note that reducing environments usually manifest under anoxic conditions, particularly in deeper lakes at a depth of approximately 10 m, substantiated by analyses of pollen and ostracode fauna [36].

All samples in this study come from the NSL1A core, which has an approximate depth of 6 m and is divided into four sections: NSL1A-1 (0–1.5 m), NSL1A-2 (1.5–3.3 m), NSL1A-3 (3.3–4.9 m), and NSL1A-4 (4.9–5.8 m). The segments ranging from 1.2 to 1.5 m and 2.6 to 3.3 m are not accessible for analysis since the cores we examined are remnants from earlier studies [36,37], and these particular intervals have been utilized in those studies. The top 6 m of the core is roughly contemporaneous with the Marine Isotope Stage (MIS) 2 full glacial event [36,37]. Dated carbonized seedpods from 2.33 m indicate an age of 23.15–22.59 cal ka BP [36,37]. Section NSL1A-4 (4.9–5.8 m) exhibits relatively low detrital sand grain contents. Moving up the core, there is a gradual increase in sand grain content, with higher values and spikes occurring in the interval between 3.8 and 4.8 m within section NSL1A-3 (3.3–4.9 m) (Figure 2) [44]. In section NSL1A-2, spanning from 1.5 m to 2.6 m, the sand content on average is closer to that observed in NSL1A-4. Detrital sand grains continue to constitute a small portion of the total composition at the base of the section until approximately 2 m, where their abundance significantly increases.

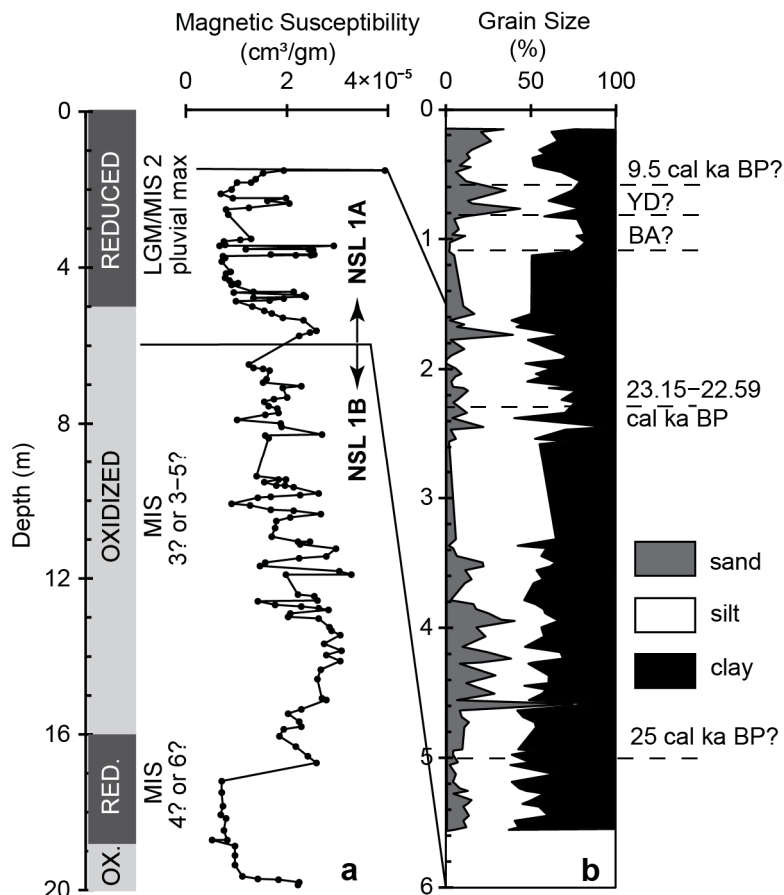


Figure 2. (a) Whole-core magnetic susceptibility [36,37] and (b) relative grain size distributions [44]. MIS = Marine Isotope Stage, LGM = Last Glacial Maximum.

3.2. Laboratory Investigation

Samples were obtained from the entire NSL1A core at 2.5 cm intervals and sent to Qingdao Sibaba Analytical Corp, Ltd. (Qingdao, China) for X-ray Fluorescence (XRF) and loss on ignition (LOI) analyses. LOI analysis first required that powdered samples were completely dried. To dry, samples within the beakers were placed in an oven at 105 °C for 2 h. After drying, samples were placed in a desiccator to cool down before weighing. Crucibles used for LOI analysis must be completely dried before weighing (accuracy ~0.0001 g) to ensure that no moisture remains that would cause an overestimation in LOI results. The total weight of each sample used for LOI analysis was approximately half a gram (0.5 g). Dried samples were transferred into crucibles and then into a muffle furnace. The furnace was heated to a temperature of 500 °C for 3 h followed by an increase to 900 °C for 3 h. Samples within crucibles were then cooled down in a desiccator and reweighed. The heating process was repeated after weighing until the weight of the crucible and powder sample remained constant. The standard measurement error for the LOI procedure at the Qingdao Sibada Analytical Corp laboratory is less than 0.40%.

Major element analyses of the samples were completed using a ZSX Primus II XRF (Rigaku Corporation, Tokyo, Japan) with a standard measurement error of less than 1.0%. The fusion bead method was used to remove any errors that may result from grain size and mineralogical effects [45]. For the fusion bead method, half a gram (0.5 g) of powdered sample was mixed with lithium tetraborate (Li₂B₄O₇) at a ratio of 1:10 and placed into a 50 mL platinum crucible. The platinum crucible acted as a mold for the bead for the rest of the process. Twenty-five milligrams (25 mg) of NH₄I solution was then added and mixed into the sample. The crucible was then placed in a high-temperature muffle furnace at 1050 °C for twenty-five minutes to melt the sample into a glass-form bead. Afterward,

the sample was removed from the furnace and left to cool down after shaking it to help facilitate homogenization and remove any trapped air bubbles [45]. After cooling, the glass bead was then removed from the mold and analyzed.

Trace and rare earth elements (REEs) were determined using a Varian 820MS ICP-MS (Varian, Inc., Palo Alto, CA, USA). To prepare samples for analysis, the samples were digested with an acid solution of HF/HNO₃. For each sample, four-hundredths of a gram (0.04 g) of powdered sample was transferred to a Teflon vessel. A total of 1.5 mL of HF and 0.5 mL of HNO₃ were then added to the vessel to dissolve the powdered samples. Vessels were tightly capped and placed into an oven at 180 °C for 12 h. Vessels were then cooled to room temperature before evaporating the acid solution. To evaporate the acid solution, caps were removed from vessels followed by heating samples to 150 °C in an oven. Following evaporation of the acid solution, 1 mL of HNO₃ and 1 mL of H₂O were added to the vessel before recapping it and placing samples into an oven. The oven was set at 150 °C for 12 h to complete the dissolution of the sampled material. The last step in the process was to cool down samples to room temperature and add DI water until the total weight was 40 g (approximately 1000 times the original weight). The standard measurement error of this method of sample preparation using the Varian 820MS ICP-MS is <5.0%. Rare earth element data are chondrite normalized to reduce the sawtooth effect, which are the variations in abundances found between REEs of odd and even atomic numbers due to the Oddo Harkins Rule [46]. The REE chondrite normalization values used in this study are obtained from Boynton [47].

4. Results

4.1. Distribution of and Variability in Major, Trace, and REE Elements

As presented in the Supplementary Materials Tables S1–S3 and Table 1, the proportions of major elements are depicted through their oxide counterparts. The samples in this study have variable major elements. SiO₂ is the most abundant oxide, ranging from 21.59% to 54.26%, with SO₃ and Al₂O₃ less so at 2.38% to 39.40% and 4.65% to 13.82%, respectively. High SiO₂ and Al₂O₃ content can be attributed to detrital quartz and clay minerals. The SO₃ content ranges widely and trends the opposite way with depth when compared to SiO₂ and Al₂O₃. Therefore, SO₃ represents the nondetrital assemblage.

Table 1. Average, maximum, and minimum deposition concentrations (%) of all major elements in the NSL1A core.

Element	Max	Min	Average	Factor (Max/Min)
SiO ₂	54.26	21.59	40.11	2.51
SO ₃	39.40	2.38	11.92	16.55
Al ₂ O ₃	13.82	4.65	9.86	2.97
CaO	21.32	1.13	8.17	18.83
MgO	8.65	2.42	5.31	3.58
Fe ₂ O ₃	7.38	1.75	4.80	4.22
Na ₂ O	6.24	1.12	3.96	5.58
K ₂ O	2.54	1.00	1.83	2.54
TiO ₂	0.57	0.15	0.40	3.87
P ₂ O ₅	0.40	0.14	0.27	2.93
MnO	0.33	0.03	0.09	13.38
LOI	18.29	6.92	13.55	2.64

Trace elements (Table 2) Sr, Ba, V, and Zn exhibit comparatively high average concentrations among all the analyzed trace elements. The Mo max/min is notably high, potentially indicating the presence of artificially introduced contaminants. The total LREE content (La, Ce, Pr, Nd, and Sm) is approximately three times greater than that of the HREE (Eu, Tb, Dy, Ho, Er, Tm, Yb, and Lu) (Table 3).

Table 2. Average, maximum, and minimum deposition concentrations (ppm) of all trace elements in the NSL1A core.

Element	Max	Min	Average	Factor (Max/Min)
Sr	1519.62	172.75	666.80	8.80
Ba	632.53	141.50	366.54	4.47
Mo	1240.22	0.82	162.77	1506.28
V	158.67	52.58	109.10	3.02
Zn	144.96	45.99	107.31	3.15
Cr	125.21	33.31	85.23	3.76
Rb	109.72	35.83	75.82	3.06
Zr	97.90	31.52	61.91	3.11
Ni	111.58	24.08	52.50	4.63
Li	70.99	24.37	51.83	2.91
B	158.53	8.84	50.53	17.93
Cu	547.73	15.16	40.74	36.12
Y	25.69	8.60	18.98	2.99
Ga	21.70	7.00	15.10	3.10
Sc	16.81	4.84	10.89	3.47
Co	15.09	4.95	10.19	3.05
Nb	13.93	4.63	10.17	3.01
As	25.50	3.08	8.49	8.29
Cs	5.86	1.79	4.21	3.27
Cd	11.20	0.70	3.23	15.95
Be	2.31	0.77	1.62	3.00
Ge	1.35	0.51	0.91	2.62

Table 3. Average, maximum, and minimum deposition concentrations (ppm) of all rare earth elements in the NSL1A core. Eu/Eu* = Eu anomalies.

Element	Max	Min	Average	Factor (Max/Min)
La	126.50	40.50	83.39	3.12
Ce	90.60	29.40	59.87	3.08
Pr	71.50	22.80	46.83	3.14
Nd	53.30	16.90	35.51	3.15
Sm	30.90	10.20	20.94	3.03
Eu	15.90	5.00	10.66	3.18
Gd	19.40	6.40	13.37	3.03
Tb	17.70	5.60	11.94	3.16
Dy	13.40	4.40	9.01	3.05
Ho	12.80	4.10	8.66	3.12
Er	11.70	3.80	7.97	3.08
Tm	11.40	3.70	7.93	3.08
Yb	11.00	3.60	7.56	3.06
Lu	10.30	3.50	7.16	2.94
La/Yb	12.20	9.70	11.03	1.26
Eu/Eu*	0.69	0.60	0.64	1.14

4.2. Paleoenvironment Proxies

The entire NSL1A core has been divided into four distinct geochemical zones based on variations in lithology and elemental composition, sequentially labeled as Zones 1 through 4 from top to bottom (Tables 4 and 5). Here, we report element ratios that serve as proxies to deduce the paleoenvironment.

The $\text{TiO}_2/\text{Al}_2\text{O}_3$, La_n/Yb_n , and Eu/Eu^* ratios serve as a valuable indicator for sediment provenance [48,49]. Temporal variation in the ratios of $\text{SiO}_2/\text{Al}_2\text{O}_3$ and $\text{Zr}/\text{Al}_2\text{O}_3$ ($\times 10^{-4}$) reflects the input of detrital influx. The Chemical Index of Alteration ($\text{CIA} = \text{Al}_2\text{O}_3 / \{\text{Al}_2\text{O}_3 + \text{CaO}^* + \text{Na}_2\text{O} + \text{K}_2\text{O}\}$) is used to determine the intensity of chemical weathering in clastic sediments [50]. Here, CaO^* only represents the CaO in silicate minerals, which can be amended by $\text{CaO}^* = \min(\text{CaO}\% - \text{P}_2\text{O}_5\% \times 10/3, \text{Na}_2\text{O}\%)$ [51,52].

Table 4. Average values of the geochemical proxies of provenance ($\text{TiO}_2/\text{Al}_2\text{O}_3$, La_n/Yb_n , Eu/Eu^*), weathering and clastic influx (CIA, $\text{SiO}_2/\text{Al}_2\text{O}_3$, $\text{Zr}/\text{Al}_2\text{O}_3$), and paleoclimate (Sr/Cu , Rb/Sr).

Zones	$\text{TiO}_2/\text{Al}_2\text{O}_3$	La_n/Yb_n	Eu/Eu^*	CIA	$\text{SiO}_2/\text{Al}_2\text{O}_3$	$\text{Zr}/\text{Al}_2\text{O}_3 \times 10^{-4}$	Sr/Cu	Rb/Sr
1	0.036	10.69	0.656	60.18	4.60	10.10	28.16	0.102
2	0.041	11.26	0.631	50.35	3.97	10.80	24.58	0.114
3	0.041	10.96	0.630	46.77	4.02	11.47	23.41	0.112
4	0.040	11.01	0.642	55.18	4.04	10.81	5.35	0.327

Table 5. Average values of the geochemical proxies of paleosalinity (SO_3 , Sr/Ba), paleoproductivity (P/Al , Ba/Al), paleowater depth (Mn/Fe), and paleoredox ($\text{V}/(\text{V} + \text{Ni})$, Ni/Co , δCe).

Zones	SO_3 (%)	Sr/Ba	$\text{P}/\text{Al} \times 10^{-4}$	$\text{Ba}/\text{Al} \times 10^{-4}$	Mn/Fe	$\text{V}/(\text{V} + \text{Ni})$	Ni/Co	δCe
1	18.05	1.95	24.72	92.41	0.020	0.672	5.21	−0.039
2	11.92	2.14	21.52	69.79	0.018	0.683	4.91	−0.039
3	12.20	2.85	21.67	61.09	0.039	0.675	5.27	−0.037
4	5.99	0.65	20.08	72.41	0.011	0.670	5.43	−0.041

The average $\text{TiO}_2/\text{Al}_2\text{O}_3$ ratio closely matches in Zone 2 (0.041), Zone 3 (0.041), and Zone 4 (0.040) but is lower in Zone 1 (0.036). The La_n/Yb_n ratio exhibits the highest average value in Zone 2 (11.26), followed by Zone 3 (10.96), Zone 4 (11.01), and Zone 1 (10.69). In terms of the average Eu/Eu^* ratios, Zone 4 has the highest value (0.656), followed by Zone 4 (0.642), Zone 2 (0.631), and Zone 3 (0.630).

The CIA values show that Zone 1 has the highest average (60.18), followed by Zone 4 (55.18), Zone 2 (50.35), and Zone 3 (46.77). In terms of $\text{SiO}_2/\text{Al}_2\text{O}_3$ ratios, Zone 1 has the highest average (4.60), followed by Zone 4 (4.04), Zone 3 (4.02), and Zone 2 (3.97). The $\text{Zr}/\text{Al}_2\text{O}_3$ ratios are highest in Zone 3 (11.47), followed by Zone 4 (10.81), Zone 2 (10.80), and Zone 1 (10.10).

The Rb/Sr [53–55] and Sr/Cu [56–60] ratios are the primary indicators of paleoclimate. The Rb/Sr ratios are highest in Zone 4 (0.327), followed by Zone 2 (0.114), Zone 3 (0.112), and Zone 1 (0.102). The averaged Sr/Cu ratio is the highest in Zone 1 (28.16), followed by Zone 2 (24.58) and Zone 3 (23.41), and is significantly lower in Zone 4 (5.35).

Paleosalinity is evaluated with the Sr/Ba ratio and SO_3 (%) [61–64]. The Sr/Ba ratios exhibit the highest average in Zone 4 (2.85), followed by Zone 2 (2.14), Zone 1 (1.95), and Zone 3 (0.65). In Zone 1, SO_3 displays the highest average value (18.05), followed by Zone 3 (12.20), Zone 2 (11.92), and Zone 4 (5.99).

The ratios of P/Al ($\times 10^{-4}$) [65–67] and Ba/Al ($\times 10^{-4}$) [68] are utilized as the key indicator of paleoproductivity. In terms of P/Al ratios, Zone 1 shows a relatively higher value (24.72), and all other zones have close values of 20.08–21.52. The Ba/Al ratios are highest in Zone 1 (92.41), followed by Zone 4 (72.41), Zone 2 (69.79), and Zone 3 (61.09).

The lake paleodepth variations and paleoredox conditions are indicated by Mn/Fe [69,70], $\text{V}/(\text{V} + \text{Ni})$, Ni/Co , [71,72] and Ce-anomaly (δCe) ratios [73]. Ce-anomaly can be calculated using the following formula: $\delta\text{Ce} = \log(3\text{Ce}_n/(2\text{La}_n + \text{Nd}_n))$. The Mn/Fe ratios are highest in Zone 3 (0.039), followed by Zone 1 (0.020), Zone 2 (0.018), and Zone 4 (0.011). The $\text{V}/(\text{V} + \text{Ni})$ ratios show close values in all zones at 0.670–0.683. The Ni/Co ratios are highest in Zone 4 (5.43), followed by Zone 3 (5.27), Zone 3 (5.21), and Zone 2 (4.91). Ce-anomaly shows close values at −0.037–0.039 in all zones.

5. Discussion

5.1. Sediment Provenance and Weathering Conditions

The $\log(\text{SiO}_2/\text{Al}_2\text{O}_3)$ versus $\log(\text{Na}_2\text{O}/\text{K}_2\text{O})$ (Figure 3) shows the majority of the samples are situated within the graywacke region with some values within the litharenite region [48]. However, it is noted that values for the $\text{Na}_2\text{O}/\text{K}_2\text{O}$ ratio are not representative of the source rock due to the presence of halite in the sediments throughout the core. When

examining the $\log(\text{SiO}_2/\text{Al}_2\text{O}_3)$ versus $\log(\text{Fe}_2\text{O}_3/\text{K}_2\text{O})$ plot [49], the majority of the samples form a closely clustered group primarily within the wacke and shale zones. This finding is consistent with the lithology of the surrounding Temblor and Caliente Range mountains, which contain a series of largely marine sedimentary sequences (Neogene, Paleogene, Cretaceous, and Jurassic) and igneous rocks that are eroded and transported into the Carrizo Plain [40].

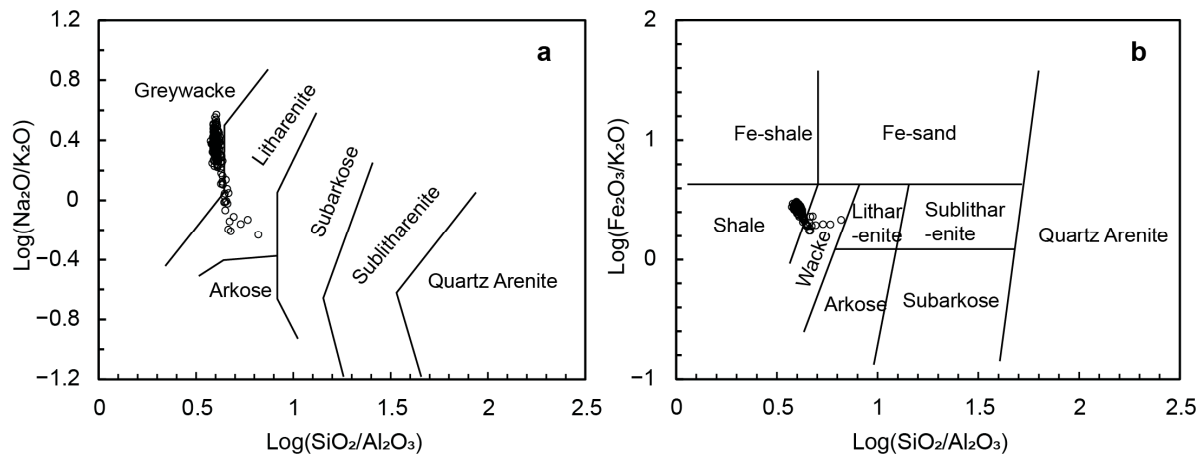


Figure 3. Geochemical classification of NSL1A samples data on (a) a $\log(\text{SiO}_2/\text{Al}_2\text{O}_3)$ vs. $\log(\text{Na}_2\text{O}/\text{K}_2\text{O})$ diagram [48] and (b) a $\log(\text{SiO}_2/\text{Al}_2\text{O}_3)$ vs. $\log(\text{Fe}_2\text{O}_3/\text{K}_2\text{O})$ diagram [49].

The concentrations of REE elements in sediments are a result of the influences of provenance, weathering, diagenesis, sediment sorting, and aqueous geochemistry of the individual elements [74]. As such, geochemical studies have concentrated on clay-rich lithologies as they contain the highest concentrations of trace elements. The ratio between La_n and Yb_n signifies LREE enrichment. For the NSL1A core, the La_n/Yb_n ratio values fall within a range of 10–12 (Table 4), indicating an LREE enrichment and a felsic source [75]. In conjunction with the La_n/Yb_n ratio, the Eu anomaly is used to identify the type of source lithology from which the sediments are derived. The results of this study show that NSL sediments are LREE enriched and have negative Eu anomalies (values between 0.6 and 0.7 for NSL sediments; Table 4). LREE enrichment and negative Eu anomalies are associated with reworked shales derived from a cratonic setting [75–78]. Thus, both REE and major element analyses provide evidence that NSL sediments are mostly derived from marine sequences in the Southern Coast Ranges.

The changes in CIA values at different depths indicate the weathering conditions in the catchment over the deposition time of the core. Generally, higher CIA values signify more intense weathering. For comparison, we simply group samples with CIA values < 60 suggesting low chemical weathering, those between 60 and 80 indicating moderate chemical weathering, and values > 80 suggesting extreme chemical weathering [50]. Although the thresholds might not directly apply to the particular study region, when considered alongside the CIA average (~51.5) in the examined core, they do provide some reasonably comparative insights into the weathering conditions over time. CIA values calculated here range between 39 and 67, indicating low to moderate chemical weathering in the sediment source regions. The few samples with >60 CIA values are concentrated from depths shallower than 45 cm or greater than 550 cm.

Analyzing the existing correlations between sediment composition and contemporary climate on Earth's surface can provide valuable insights into understanding past climatic conditions. However, challenges arise when utilizing geochemical and mineralogical indices as proxies for climate [79,80]. For example, the composition of detrital daughter sediments is primarily influenced by the parent rock's composition. Additionally, even in similar source-area geologies, sediment composition is heavily reliant on the grain size of the generated sediments. It seems that the composition of clay is somewhat less

influenced by the distinction between felsic and mafic provenance compared to coarser detritus [80]. Most of the samples in this study are tightly clustered, predominantly within the wacke and shale zones (Figure 3). Analysis of grain size indicates that the sediments are mainly composed of clay and silt (Figure 2) [44]. The geological context in this study area is primarily characterized by marine or nonmarine sedimentary rocks. Notably, the age of the studied Soda Lake sediments is more recent than the period when the western North American continent margin underwent a transition into a strike-slip configuration during the Miocene. So, it can be anticipated that the influx of sediments into the lake is predominantly influenced by climate conditions rather than tectonic activities. Additionally, being a relatively small and geologically isolated region, its sediment provenance may remain relatively constant. Consequently, it can be asserted that the variations in proxies in this study more accurately capture climatic influences rather than being significantly influenced by provenance effects. As previously stated, the nearly identical LREE values in the four zones (Table 4) provide additional support that the influence of provenance change is minimal.

The changing $\text{SiO}_2/\text{Al}_2\text{O}_3$ and $\text{Zr}/\text{Al}_2\text{O}_3$ ratios over time indicate the contribution of quartz and zircon [81–84], respectively. These ratios serve as indicators of clastic input, whether it is through aeolian processes or the transport of aeolian sediments during periods of precipitation. The $\text{SiO}_2/\text{Al}_2\text{O}_3$ and $\text{TiO}_2/\text{Al}_2\text{O}_3$ ratios exhibit inverse variations along the depth profile. An obvious abrupt change occurs at 82.5 cm from the top of the core (Figure 4). The variation in $\text{TiO}_2/\text{Al}_2\text{O}_3$ values could potentially elucidate alterations in the mafic components within the sedimentary system [85]. Nonetheless, this shift observed from 82.5 cm to the surface is more likely attributable to the warming and increasingly humid conditions in the Holocene. These climatic changes intensified chemical weathering in the catchment (Figure 4), resulting in the depletion of Ti and enrichment of Si in the source sediments. This transition is also reinforced by a noticeable decrease up core in the concentrations of trace metals such as Rb, Ba, Zn, and Cu (Figure 4). Additional mineralogical analysis is necessary to delve deeper into understanding and resolving this transition.

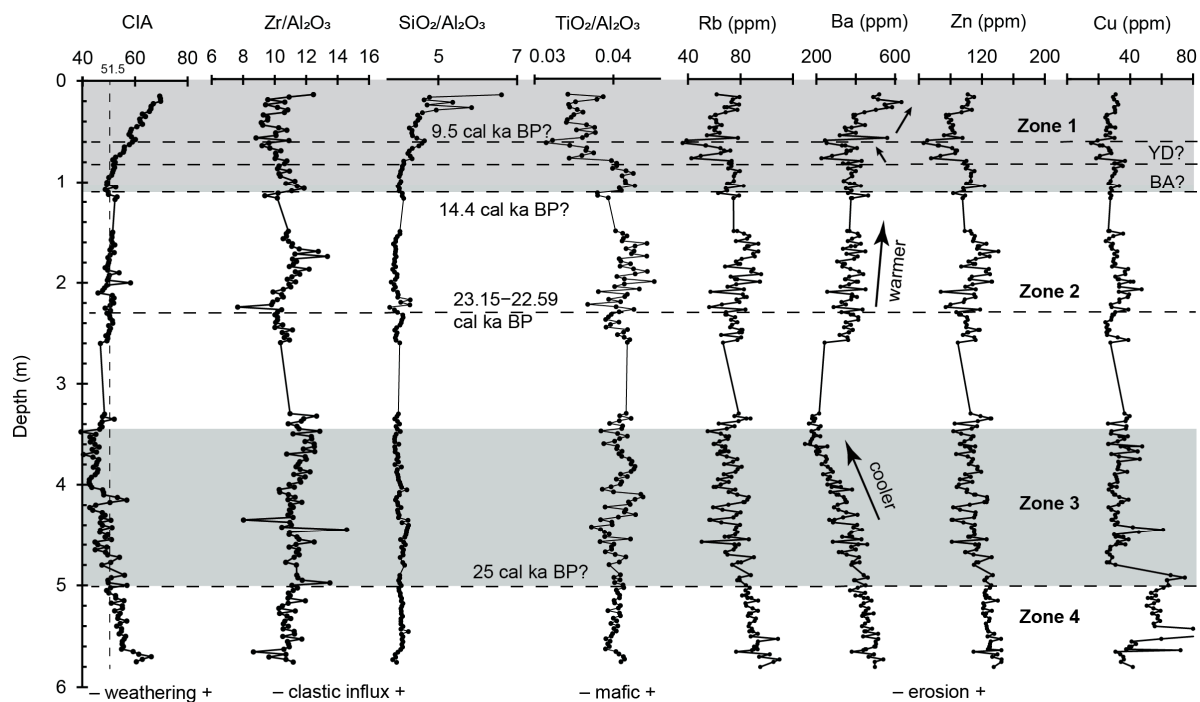


Figure 4. Variations in CIA, $\text{Zr}/\text{Al}_2\text{O}_3$, $\text{SiO}_2/\text{Al}_2\text{O}_3$, and $\text{TiO}_2/\text{Al}_2\text{O}_3$ and the distribution of Rb, Ba, Zn, and Cu (in ppm) in the geochemical zones along the depth profile. BA = Bølling–Allerød, YD = Younger Dryas.

5.2. Paleoclimate

The Rb/Sr ratio serves as an effective indicator of chemical weathering processes and consequently provides insight into depositional environment and paleoclimate changes. The Rb/Sr ratio has become an ideal indicator in the study of regional climate environment evolution [53–55]. For instance, Chang et al. note that the Rb/Sr ratio responds to precipitation changes in a manner similar to pollen and ostracod assemblages, affirming its suitability as a precipitation proxy [54].

A high Rb/Sr ratio typically signifies warm and humid climates. This is because Rb remains relatively stable while Sr is often leached away due to heavy precipitation. Conversely, a low Rb/Sr ratio points to arid climatic conditions, as minimal Sr is lost in environments with low precipitation. At present, few geochemical studies have explored Rb/Sr in lake sediments from the Southwestern North America (SWNA) region for comparative analysis. The established threshold for Rb/Sr, linked to climate changes in the eastern and central regions of China where monsoon influences are investigated, is defined as 0.45 [86–89]. By applying a comparable threshold Rb/Sr value of 0.45, as employed in the monsoon-influenced regions of eastern and central China, it can be inferred that the climate in this study region was predominantly dry and arid across all four zones. However, it is essentially notable that these thresholds cannot be universally applied. In this study, we rely on the average Rb/Sr value of 0.16, indicating climate variations across different sections. The higher Rb/Sr values observed in Zone 4 imply a climate that is relatively more humid when compared to the other zones (Figure 5).

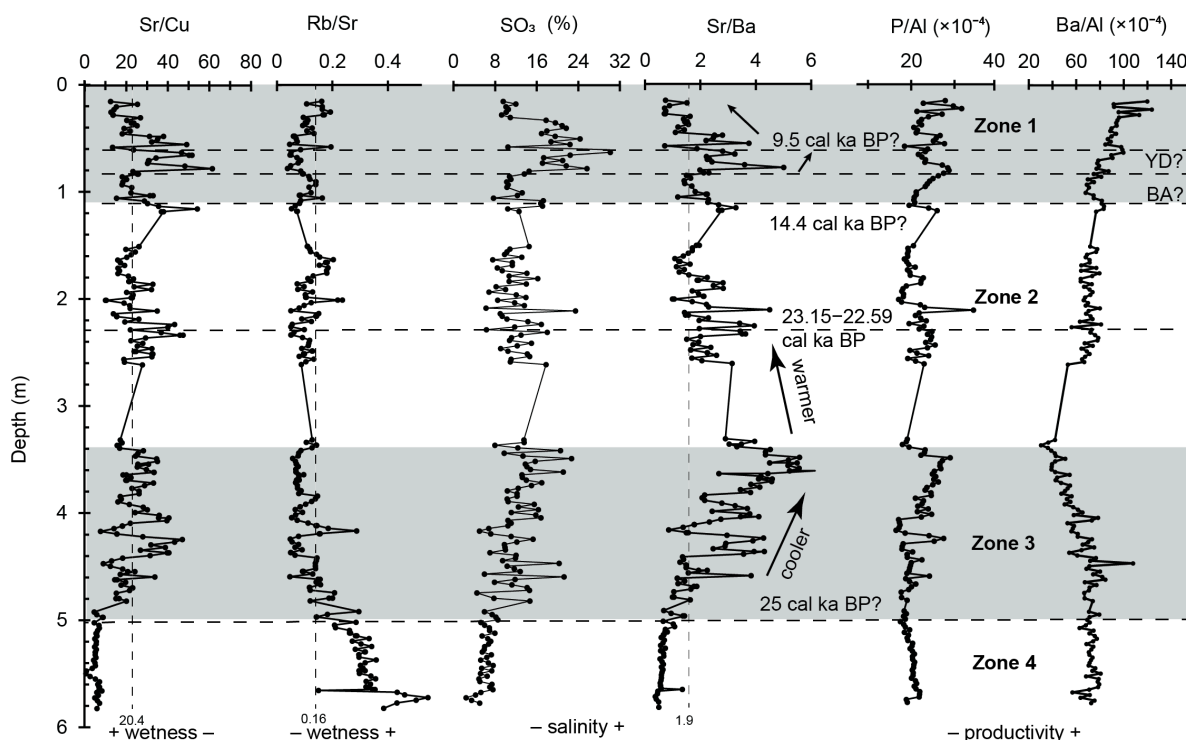


Figure 5. Variations in Sr/Cu, Rb/Sr, SO₃ (in %), Sr/Ba, P/Al, and Ba/Al in the geochemical zones along the depth profile. BA = Bølling–Allerød, YD = Younger Dryas.

The Sr/Cu ratio has also been commonly used to characterize paleoclimatic conditions [56–60]. Increasing Sr/Cu values suggest that the climate varies from warm-humid to hot-dry conditions [56,57]. Lerman proposed that low Sr/Cu ratios between 1.3 and 5.0 reflect warm and humid climates and that ratios greater than 5.0 correspond to hot and dry climates [56]. The Sr/Cu ratios in Zone 4 have an average of 5.35, indicating a relatively humid climate during the depositional period (Table 4; Figure 5). Zones 1–3 have higher average Sr/Cu ratios (>20), and the ratio shows variation with depth. Yet, as previously

noted, these thresholds are not universally applicable. Taking into account fluctuations around the average Sr/Cu ratio (~20.4), it can be deduced that the Soda Lake watershed experienced alternating semiarid and arid conditions during the depositional periods in Zone 1, 2, and 3.

5.3. Paleosalinity and Paleoproductivity

The Sr/Ba ratio is widely employed as an indicator for reconstructing paleosalinities and the corresponding climatic conditions. It is particularly linked to the salinization of the water column, which is strongly influenced by evaporation in arid and semiarid climates [61–63]. Commonly, Sr exhibits a stronger migration compared to Ba. Sr precipitation only initiates when salinity levels are elevated [90,91]. Consequently, salinity can be classified into three distinct ranges: freshwater (Sr/Ba < 0.5), brackish water (Sr/Ba 0.5–1), and saltwater (Sr/Ba > 1) [64]. Accordingly, the entire NSL1A section deposited in either the brackish water (Zone 4 and top half section of Zone 1) or saltwater environments (Zones 2 and 3 and bottom half of Zone 1). The trend of Sr/Ba is comparable to the abundance of SO₃, which indicates that the high salinization of the water column during deposition was controlled by evaporation under arid and semiarid climatic conditions (Figure 5). There are also significant covariations between Sr/Ba ratios and Sr/Cu ratios, which suggests that climatic conditions exert control over Sr/Ba ratios in this context. Therefore, the notable changes in paleosalinity, transitioning from a brackish water environment to a saltwater environment and then back to a brackish water environment, are closely linked to variations in climate.

P in sediments plays a crucial role as a nutrient element, impacting the productivity of the water column [92,93]. Predominantly, it exists in the form of organic and detrital phosphorus. Nevertheless, it is only the organic P in sediments that can be utilized to reconstruct the productivity of the water column [65–67]. The P₂O₅ abundances in the NSL1A core can be correlated with SiO₂ (R = 0.60), Al₂O₃ (R = 0.56) and TiO₂ (R = 0.49), which indicates that most phosphorus is associated with detrital materials. To eliminate the effects of terrigenous input and to represent paleoproductivity, the Al-normalized abundance of P (P/Al) is evaluated (Figure 5). The P/Al ratios of samples from all zones show relatively low values, ranging from 20.08 to 24.71. These results suggest that the sediments were deposited in environments with relatively low paleoproductivity.

Ba content is another good geochemical indicator of paleoproductivity. Elevated Ba content is associated with increased productivity [68]. This correlation arises from the precipitation of Ba²⁺ as BaSO₄, forming a combination with SO₄²⁻ on the surface of organic matter [94,95]. Consequently, there is a positive correlation between the barite accumulation rate and primary productivity. To eliminate the effect of detail barium, the Ba/Al ratio is commonly used to qualitatively estimate primary productivity [96]. In this study, the Al-normalized abundances of Ba (Ba/Al) along depths are comparable to the variation pattern of Ba concentrations (Figures 4 and 5). The average ratios of Ba/Al vary from 61.09 to 92.41 in all zones (Table 5). The lower values exist in Zone 3 (61.09) and Zone 2 (69.79), indicating a relatively lower productivity than that of Zone 1 and Zone 4. The vertical variation in the Ba/Al ratios does not fully correspond to that of the P/Al ratios, which may be due to the interaction of multiple factors affecting the Ba taken up by sediments in the water column, such as redox conditions, particulate shuttles, aqueous chemistry, and organic matter concentrations.

5.4. Paleoredox Environment and Lake Water Depth

Trace elements are sensitive to redox in sediments and controlled by the redox conditions during deposition; therefore, the paleoredox environment can be determined based on the contents or ratios of trace elements such as V, Ni, Cr, Co, Fe, and Zn [97]. Specifically, V is inclined to precipitation in anoxic/euxinic environments and dissolution in oxic environments, while Ni is more stable than V in both environments [98,99]. Therefore, the ratios of V/(V + Ni) and Ni/Co can serve as indicators of redox conditions [71,72]. A high

$V/(V + Ni)$ value (≥ 0.84) reflects water column stratification and indicates an anaerobic reduction environment, whereas a range of 0.6–0.84 indicates weak water column stratification and an anoxic environment, and low values (< 0.6) indicate an oxygen-rich environment. Moreover, $Ni/Co < 5.0$ reflects an oxygenic environment, Ni/Co of 5.0–7.0 signifies a sub-oxic to dysoxic environment, and $Ni/Vo > 7.0$ indicates a reducing environment. The ratios of $V/(V + Ni)$ and Ni/Co are 0.67–0.683 and 4.91–5.43, respectively, in all zones (Table 5), which suggest that the NSL1A core is identified to be mainly formed in a subreduction environment (Figure 6).

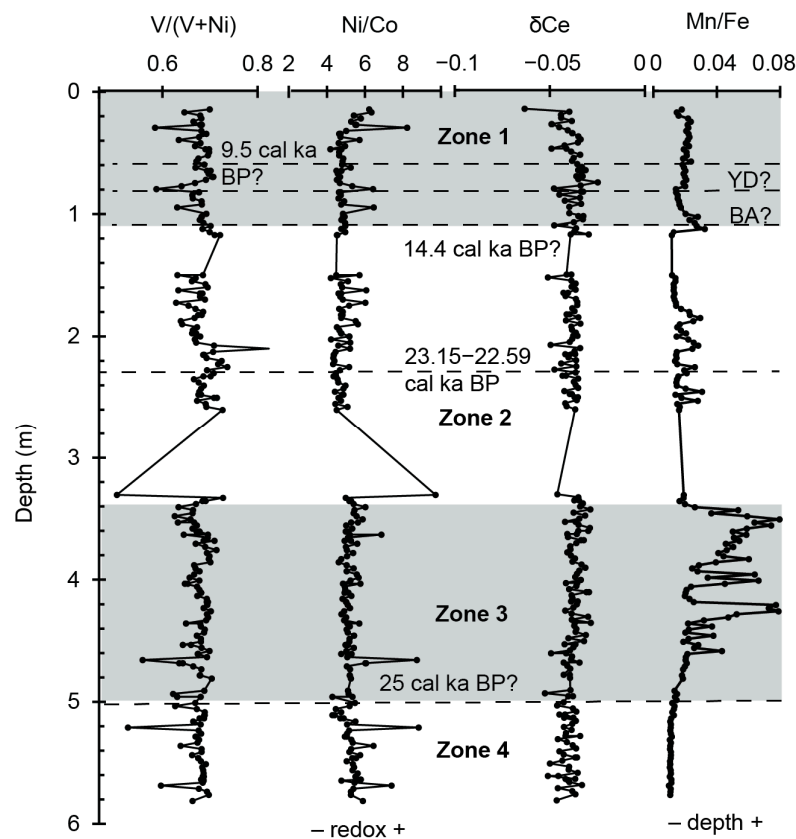


Figure 6. Variations in $V/(V + Ni)$, Ni/Co , δCe , and Mn/Fe in the geochemical zones along the depth profile. BA = Bølling–Allerød, YD = Younger Dryas.

Ce-anomaly (δCe) in rare earth elements is sensitive to the oxidative-reductive conditions of the depositional environment. When Ce-anomaly is greater than -0.10 , it indicates Ce enrichment and therefore a reducing environment. A Ce-anomaly value of less than -0.10 indicates Ce depletion and therefore an oxidizing environment [73]. In all four zones, Ce-anomaly shows little variance with values averaging from -0.041 to -0.037 , with a relatively low average value of -0.041 only in Zone 4. Obviously, Ce-anomaly values support a reducing deposition environment during the deposition of the NSL1A core (Figures 2 and 6).

Within the lake environment, elements with variable valence, such as Fe and Mn, exhibit distinct behaviors. Fe^{2+} is more susceptible to oxidation compared to Mn^{2+} , while Mn hydroxide undergoes easier reduction than Fe oxide. Elevated Fe/Mn ratios are indicative of more reducing conditions, often associated with a decrease in lake water depth. Consequently, Fe/Mn ratios have been employed as a proxy indicator for estimating lake water depth [69,70]. The concentration levels of these elements in the NSL1A core imply fluctuations in water depth across various zones. However, the higher Mn/Fe ratios in Zone 3 indicate a relatively increasing water depth during the deposition time (Figure 6). Some small water depth excursions can be observed in Zone 2.

5.5. Evolution of the Paleosedimentary Environment

The NSL1A core records the sedimentary evolution of the Soda Lake watershed. Based on the variation in proxies for paleoweathering, paleoclimate, paleosalinity, paleoproductivity, paleoredox, and water depth, the evolution of the sedimentary environment is reconstructed in the study area, which is discussed along four geochemical zones.

Zone 4 (5.0–5.8 m): Variations in the lake's water depth are primarily influenced by seasonal precipitation patterns in this pluvial lake. During periods of heavy rainfall and flooding, significant amounts of coarse detrital materials are typically introduced into the lake through turbidity processes. Hence, a significant presence of coarse-sized particles indicates heightened water inflow into the lake, particularly during seasons characterized by heavy precipitation. The relatively low and constant sand and silt content in this zone (Figure 2) indicates stable hydroclimatic conditions during the deposition period of this zone.

This zone is characterized by relatively moderate weathering and low salinity, suggesting a relatively warm and relatively humid environment with relatively fresh and unstratified water in the lake (Figure 3). The magnetic susceptibility and abundances of trace elements (Rb, Ba, Zn, Cu) are comparable in this zone, with lower Mn/Fe ratios (Figures 4 and 6). This suggests that the water depth is relatively shallow. The presence of fresh, unstratified water and shallow water depth is also supported by the oxidized lithology [36].

The NSL1A sediments were deposited during the MIS1 and MIS2 stages [37]. Rhodes et al. identified that the lake high stand persisted from approximately 25 to 21 cal ka BP [36]. Consequently, the age of the top boundary of Zone 4 can be estimated to be around 25 cal ka BP. This zone corresponds to the regional glacial megadrought (27.6–25.7 cal ka BP) [20,100]. The low productivity in this zone indicates that the megadrought may be a regional phenomenon in the NWSA region. There remains much work to be done in order to better constrain the occurrence of this event and further understand the dynamics and potential factors causing low water productivity during this relatively humid period.

Zone 3 (3.35–5.0): The LGM is between 26.5 and 19 cal ka BP [101]. This zone encompasses the early half of this interval and the high lake stand [36]. It is characterized by rising salinity and decreasing wetness and trace element abundances (Figures 4 and 5). The sand and silt content shows an increase when compared to Zone 4. Low weathering conditions caused the decrease in erosion and reduced trace element inflow into the lake (Figure 4). The increased sand content might be the aftermath of transient flood events, which can be explained by the northerly migration in the mean position of the westerly storm tracks. Lake levels in the Mojave River Basin suggest storm tracks were frequently directed at 32°–34° N, causing an increase in winter flood frequency and the coexistence of lakes during the LGM [102]. The winter flood inflow into the lake increased the lake level transiently, as shown by the Mn/Fe high spikes in this zone (Figure 6). A lake high stand is commonly considered to be associated with low evaporative conditions. However, the salinity gradually increased in this zone, which might be due to the significantly lower temperature and the relatively dry conditions. This might have favored the freezing out of Sr in sediments. The slight increase in productivity could have been caused by the less evaporative conditions. A colder climate could sustain and promote mesic vegetation, even under conditions of less moisture [20].

Zone 2 (1.075–3.35 m) is characterized by a gradual decrease in salinity and a relatively higher weathering CIA, indicating a slowly warming climate. The lower section (2–3.35 m) encompasses the latter half of the Last Glacial Maximum (LGM) and a relatively stable high lake stand, which can be observed from the relatively low sand content and constant abundances of detrital trace metal elements (Figures 2 and 4). The upper section (1.075–2 m) may encapsulate Heinrich Stadial 1 (17.5–15 cal ka BP), a generally cooler period in the Northern Hemisphere [103]. However, the gradual decrease in salinity and slight increase in wetness, detrital trace metals, and paleoproductivity suggest a trend toward wetter conditions and a long-term shift from cooler to warmer periods [20].

Despite the association with a cooler period, Zone 2 exhibits a nuanced pattern. Salinity gradually decreases, accompanied by subtle increases in wetness, detrital trace metals, and paleoproductivity. These changes suggest a multifaceted environmental evolution: a trend towards wetter conditions alongside a prolonged shift from cooler to warmer periods.

Zone 1 (0.15–1.075 m): This zone (14.4 cal ka BP—Holocene) likely covers the Lateglacial to Holocene transition interval as well as Early and Middle Holocene. This transitional interval is prominently featured as a period of significant hydrologic and ecologic variability [19]. The contrasting trends in salinity and wetness between the intervals 0.575–0.825 m and 0.825–1.075 m seems to correspond to the shift from a rapid warming during the Bølling–Allerød (BA) to a rapid cooling associated with the Younger Dryas (YD) (Figure 7) [104,105]. Rhodes et al. identified at least one intermediate stand around 9.5 cal ka BP when the lake shrank to the modern Soda Lake pan [36]. This date can be associated with a depth of 0.825 m, where there is a decrease in sand and silt content, indicating a reduction in precipitation-related runoff and a shift to a shallow and low-energy lake environment due to weakening hydroclimatic dynamics. Moving up the core, the weathering CIA increases together with shallowing water depth, bringing more detrital trace elements to the lake. Paleoproductivity rises due to a warmer climate (Figures 4 and 5), which is also supported by the comparison between the modern pollen record and the most recent glacial maximum record from core NSL1 [36]. Elevated $\text{SiO}_2/\text{Al}_2\text{O}_3$ and $\text{Zr}/\text{Al}_2\text{O}_3$ ratios, along with a gradual rise in sand content above 0.825 m, indicate the influx of coarse quartz and zircon into the lake basin. As previously discussed, the $\text{TiO}_2/\text{Al}_2\text{O}_3$ values, which are relatively lower from 82.5 cm to the surface compared to the deeper portion, further support the notion of warming and increasingly humid conditions during the Holocene. Additional age-dating data are essential for comparing the uppermost section in this zone with the previous findings from the study conducted on the South Soda Lake core [38], which spans from 4.0 cal ka BP to the present day, due to the absence of age controls in the existing data.

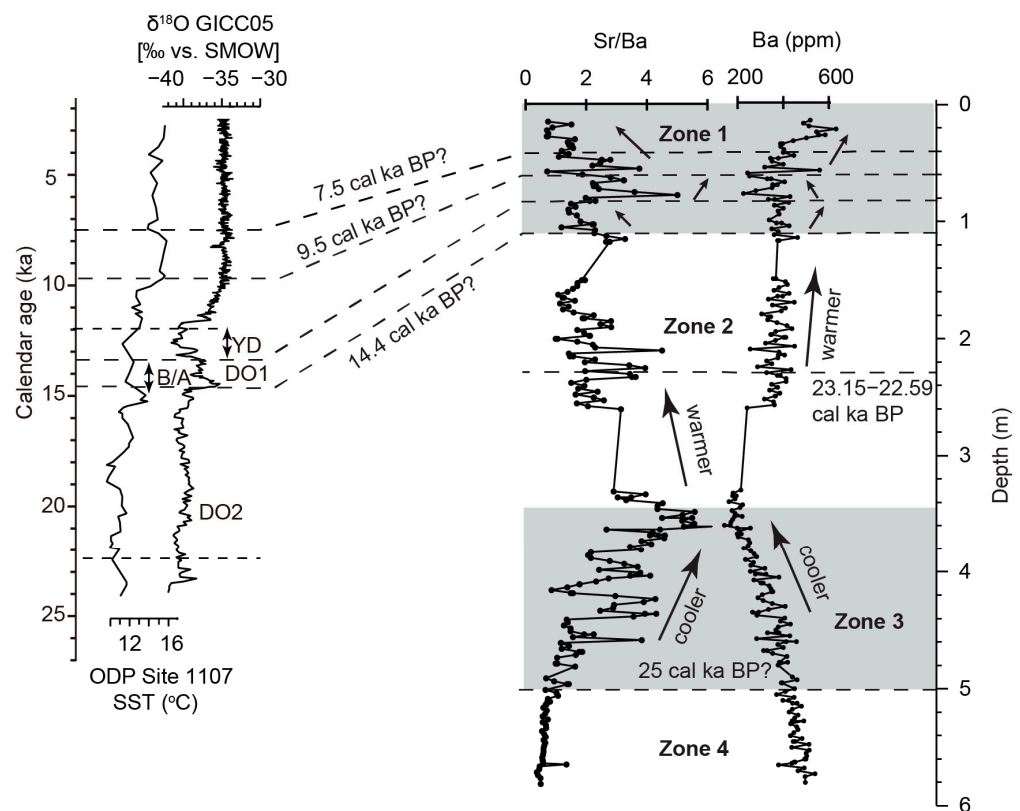


Figure 7. Comparison and correlation of proxies Ba and Sr/Ba to the variations in Pacific sea surface temperature [106] and the ratio of stable isotopes oxygen-18 and oxygen-16 ($\delta^{18}\text{O}$) in the Greenland

Ice Core Chronology 2005 (GICC05) ice core [107]. BA = Bølling–Allerød, YD = Younger Dryas, DO = Dansgaard–Oeschger event, SST = sea surface temperature, and SMOW = standard mean ocean water.

6. Conclusions

Both major and REE element analyses provide evidence that Soda Lake sediments are mostly derived from marine sequences in the Southern Coast Ranges of California. The variation in proxies for paleoweathering, paleoclimate, paleosalinity, paleoproductivity, paleoredox, and water depth is utilized to reconstruct the evolution of the sedimentary environment. The values of the CIA indicate low to moderate chemical weathering in the sediment source regions. According to paleoredox proxies, the NSL1A core is identified as having mainly formed in a subreduction environment. The NSL1A core is divided into four zones based on the features of the proxies.

1. Zone 4 (5.0–5.8 m) of the sediment core indicates stable hydroclimatic conditions with low and constant sand and silt content, suggesting a warm and relatively humid environment. This zone corresponds to the regional glacial megadrought (27.6–25.7 cal ka BP), showing moderate weathering, low salinities, and a relatively fresh, shallow, unstratified lake water environment.
2. Zone 3 (3.35–5.0 m) represents the early half of the LGM interval and a high lake stand. Characterized by increasing sand and silt content, rising salinity, and reduced wetness and trace element abundances, this zone reflects low weathering conditions, leading to decreased erosion and trace element inflow into the lake. The elevated sand content suggests postflood events due to the northerly migration of westerly storm tracks.
3. Zone 2 (1.075–3.35 m) reveals nuanced changes and demonstrates a gradual decrease in salinity and a relatively higher CIA, indicating a slowly warming climate. The lower section (2–3.35 m) represents the latter half of the LGM interval and shows a stable high lake stand, evident from low sand content and constant detrital trace metal abundances. The upper section (1.075–2 m) corresponds to Heinrich Stadial 1 (17.5–15 cal ka BP), a generally cooler period in the Northern Hemisphere.
4. Zone 1 (0.15–1.075 m) spans the Lateglacial to Holocene transition as well as Early and Middle Holocene, marked by significant hydrologic and ecologic variability including rapid warming during the BA to rapid cooling associated with the YD. Around 9.5 cal ka BP, an intermediate stand occurred at a depth of 0.825 m, indicating reduced precipitation-related runoff and a shift to a shallow, low-energy lake environment due to weakening hydroclimatic dynamics. Further up core, lake records indicate a warmer Early and Middle Holocene climate.

Supplementary Materials: The following supporting information can be downloaded at <https://www.mdpi.com/article/10.3390/min14030211/s1>, Table S1: Distribution of the variability in major elements in the NSL1A core; Table S2: Distribution of the variability in trace elements in the NSL1A core; Table S3: Distribution of the variability in chondrite-normalized rare earth elements in the NSL1A core.

Author Contributions: Conceptualization, A.R., J.G. and W.K.; investigation, A.R.; interpretation, A.R., J.G. and K.O.; resources, J.G.; writing—original draft, A.R. and J.G.; writing—review and editing, K.O., W.K. and J.G.; visualization, A.R. and J.G.; supervision, J.G.; project administration, W.K.; funding acquisition, W.K. and J.G. All authors have read and agreed to the published version of the manuscript.

Funding: This research was funded by the U.S. National Science Foundation, grant number NSF HRD-1547784.

Data Availability Statement: The data presented in this study are contained within the article.

Acknowledgments: The authors acknowledge Rob Negrini at the California State University, Bakersfield for providing core samples and Xuebo Yin at the Institute of Oceanology, Chinese Academy of

Sciences for his help with elemental analyses. The authors also acknowledge the practical support of California State University, Bakersfield and the U.S. National Science Foundation.

Conflicts of Interest: The authors declare no conflicts of interest.

References

1. Oster, J.L.; Ibarra, D.E.; Winnick, M.J.; Maher, K. Steering of westerly storms over western North America at the Last Glacial Maximum. *Nat. Geosci.* **2015**, *8*, 201–205. [\[CrossRef\]](#)
2. Seager, R.; Vecchi, G.A. Greenhouse warming and the 21st-century hydroclimate of southwestern North America. *Proc. Natl. Acad. Sci. USA* **2010**, *107*, 21277–21282. [\[CrossRef\]](#) [\[PubMed\]](#)
3. Ding, Z.L.; Yang, S.L.; Sun, J.M.; Liu, T.S. Iron geochemistry of loess and red clay deposits in the Chinese Loess Plateau and implications for long-term Asian monsoon evolution in the last 7.0 Ma. *Earth Planet. Sci. Lett.* **2001**, *185*, 99–109. [\[CrossRef\]](#)
4. Gallet, S.; Jahn, B.-M.; Torii, M. Geochemical characterization of the Luochuan loess-paleosol sequence, China, and paleoclimatic implications. *Chem. Geol.* **1996**, *133*, 67–88. [\[CrossRef\]](#)
5. Shilling, A.S.; Colcord, D.E.; Karty, J.; Hansen, A.; Freeman, K.H.; Njau, J.K.; Stanistreet, I.G.; Stollhofen, H.; Schick, K.D.; Toth, N.; et al. Biogeochemical evidence from OGCP Core 2A sediments for environmental changes preceding deposition of Tuff IB and climate transitions in Upper Bed I of the Olduvai Basin. *Palaeogeogr. Palaeoclimatol. Palaeoecol.* **2020**, *555*, 109824. [\[CrossRef\]](#)
6. Wang, C.; Bendle, J.A.; Zhang, H.; Yang, Y.; Liu, D.; Huang, J.; Cui, J.; Xie, S. Holocene temperature and hydrological changes reconstructed by bacterial 3-hydroxy fatty acids in a stalagmite from central China. *Quat. Sci. Rev.* **2018**, *192*, 97–105. [\[CrossRef\]](#)
7. Anderson, R.S. Holocene forest development and paleoclimates within the central Sierra Nevada, California. *J. Ecol.* **1990**, *78*, 470–489. [\[CrossRef\]](#)
8. Anderson, R.S.; Smith, S.J. Late Wisconsin paleoecologic record from Swamp Lake, Yosemite National Park, California. *Quat. Res.* **1992**, *38*, 91–102.
9. Anderson, R.S.; Smith, S.J. Paleoclimatic interpretations of meadow sediment and pollen stratigraphies from California. *Geology* **1994**, *22*, 723–726. [\[CrossRef\]](#)
10. Brunelle, A.; Anderson, R.S. Sedimentary charcoal as an indicator of late Holocene drought in the Sierra Nevada, California, and its relevance to the future. *Holocene* **2003**, *13*, 21–28. [\[CrossRef\]](#)
11. Koehler, P.A.; Anderson, R.S. Thirty thousand years of vegetation changes in the Alabama Hills, Owens Valley, California. *Quat. Res.* **1995**, *43*, 238–248. [\[CrossRef\]](#)
12. Mensing, S.A. Late-glacial and early Holocene vegetation and climate change near Owens Lake, eastern California. *Quat. Res.* **2001**, *55*, 57–65. [\[CrossRef\]](#)
13. Oster, J.L.; Montañez, I.P.; Sharp, W.D.; Cooper, K.M. Late Pleistocene California droughts during deglaciation and Arctic warming. *Earth Planet. Sci. Lett.* **2009**, *288*, 434–443. [\[CrossRef\]](#)
14. Bird, B.W.; Kirby, M.E. An alpine lacustrine record of early Holocene North American Monsoon dynamics from Dry Lake, southern California (USA). *J. Paleolimnol.* **2006**, *35*, 179–192. [\[CrossRef\]](#)
15. Filippelli, G.M.; Souch, C. Effects of climate and landscape development on the terrestrial phosphorus cycle. *Geology* **1999**, *27*, 171–174. [\[CrossRef\]](#)
16. Filippelli, G.M.; Carnahan, J.W.; Derry, L.A.; Kurtz, A. Terrestrial paleorecords of Ge/Si cycling derived from lake diatoms. *Chem. Geol.* **2000**, *168*, 9–26. [\[CrossRef\]](#)
17. Kirby, M.E.; Lund, S.P.; Poulsen, C.J. Hydrologic variability and the onset of modern El Niño-Southern Oscillation: A 19250-year record from Lake Elsinore, southern California. *J. Quat. Sci.* **2005**, *20*, 239–254. [\[CrossRef\]](#)
18. Kirby, M.E.; Lund, S.P.; Anderson, M.A.; Bird, B.W. Insolation forcing of Holocene climate change in Southern California: A sediment study from Lake Elsinore. *J. Paleolimnol.* **2007**, *38*, 395–417. [\[CrossRef\]](#)
19. Kirby, M.E.; Feakins, S.J.; Bonuso, N.; Fantozzi, J.M.; Hiner, C.A. Latest Pleistocene to Holocene hydroclimates from Lake Elsinore, California. *Quat. Sci. Rev.* **2013**, *76*, 1–15. [\[CrossRef\]](#)
20. Kirby, M.E.; Heusser, L.; Scholz, C.; Ramezan, R.; Anderson, M.A.; Markle, B.; Rhodes, E.; Glover, K.C.; Fantozzi, J.; Hiner, C.; et al. A late Wisconsin (32–10k cal a BP) history of pluvials, droughts, and vegetation in the Pacific southwest United States (Lake Elsinore, CA). *J. Quat. Sci.* **2018**, *33*, 238–254. [\[CrossRef\]](#)
21. Davis, O.K. Rapid climatic change in coastal southern California inferred from pollen analysis of San Joaquin Marsh. *Quat. Res.* **1992**, *37*, 89–100. [\[CrossRef\]](#)
22. Blunt, A.; Negrini, R.M. Lake levels for the past 19,000 years from the TL05-4 cores, Tulare Lake, California, USA: Geophysical and geochemical proxies. *Quat. Int.* **2015**, *387*, 122–130. [\[CrossRef\]](#)
23. Negrini, R.M.; Wigand, P.E.; Draucker, S.; Gobalet, K.; Gardner, J.K.; Sutton, M.Q.; Yohe, R.M. The Rambla highstand shoreline and the Holocene lake level history of Tulare Lake, California, USA. *Quat. Sci. Rev.* **2006**, *25*, 1599–1618. [\[CrossRef\]](#)
24. Bacon, S.N.; Burke, R.M.; Pezzopane, S.K.; Jayko, A.S. Last glacial maximum and Holocene lake levels of Owens Lake, eastern California, USA. *Quat. Sci. Rev.* **2006**, *25*, 1264–1282. [\[CrossRef\]](#)
25. Kirby, M.E.; Knell, E.J.; Anderson, W.T.; Lachniet, M.S.; Palermo, J.; Eeg, H.; Hiner, C.A. Evidence for insolation and Pacific forcing of late glacial through Holocene climate in the Central Mojave Desert (Silver Lake, CA). *Quat. Res.* **2015**, *84*, 174–186. [\[CrossRef\]](#)

26. Wells, S.G.; Brown, W.J.; Enzel, Y.; Anderson, R.Y.; McFadden, L.D. Late Quaternary geology and paleohydrology of pluvial Lake Mojave, Southern California. In *Paleoenvironments and Paleohydrology of the Mojave and Southern Great Basin Deserts*; Enzel, Y., Lancaster, N., Eds.; Geological Society of America: Boulder, CO, USA, 2003; Volume 368, pp. 79–114.
27. Anderson, L.A.; Berkelhammer, M.; Barron, J.A.; Steinman, B.A.; Finney, B.P.; Abbott, M.B. Lake oxygen isotopes as recorders of North American Rocky Mountain hydroclimate: Holocene patterns and variability at multidecadal to millennial timescales. *Glob. Planet. Change* **2016**, *137*, 131–148. [[CrossRef](#)]
28. Benson, L. Records of millennial-scale climate change from the Great Basin of the western United States. In *Mechanisms of Global Climate Change at Millennial Time Scales*; Clark, P.U., Webb, R.S., Keigwin, L.D., Eds.; American Geophysical Union: Washington, DC, USA, 1999; Volume 112, pp. 203–225.
29. Birks, H.H.; Birks, H.J.B. Multi-proxy studies in palaeolimnology. *Veg. Hist. Archaeobot.* **2006**, *15*, 235–251. [[CrossRef](#)]
30. Kirby, M.E.; Lund, S.P.; Bird, B.W. Mid-Wisconsin sediment record from Baldwin Lake reveals hemispheric climate dynamics (Southern CA, USA). *Palaeogeogr. Palaeoclimatol. Palaeoecol.* **2006**, *241*, 267–283. [[CrossRef](#)]
31. Kirby, M.E.; Zimmerman, S.R.H.; Patterson, W.P.; Rivera, J.J. A 9170-year record of decadal-to-multi-centennial scale pluvial episodes from the coastal Southwest United States: A role for atmospheric rivers? *Quat. Sci. Rev.* **2012**, *46*, 57–65. [[CrossRef](#)]
32. Noble, P.J.; Ball, G.I.; Zimmerman, S.H.; Maloney, J.; Smith, S.B.; Kent, G.; Driscoll, N. Holocene paleoclimate history of Fallen Leaf Lake, Ca., from geochemistry and sedimentology of well-dated sediment cores. *Quat. Sci. Rev.* **2016**, *131*, 193–210. [[CrossRef](#)]
33. Reheis, M.C.; Miller, D.M.; McGeehin, J.P.; Redwine, J.R.; Oviatt, C.G.; Bright, J. Directly dated MIS3 lake-level record from Lake Manix, Mojave Desert, California, USA. *Quat. Res.* **2015**, *83*, 187–203. [[CrossRef](#)]
34. Street, J.H.; Anderson, R.S.; Paytan, A. An organic geochemical record of Sierra Nevada climates since the LGM from Swamp Lake, Yosemite. *Quat. Sci. Rev.* **2012**, *40*, 89–106. [[CrossRef](#)]
35. Glover, K.C.; Chaney, A.; Kirby, M.E.; Patterson, W.P.; MacDonald, G.M. Southern California vegetation, wildfire, and erosion had nonlinear responses to climatic forcing during marine isotope stages 5–2 (120–15 ka). *Paleoceanogr. Paleoclimatol.* **2020**, *35*, e2019PA003628. [[CrossRef](#)]
36. Rhodes, D.D.; Negrini, R.M.; Arrowsmith, J.R.; Wigand, P.E.; Forman, S.L.; Palacios-Fest, M.R.; Davis, O.K. Geomorphic and sedimentologic evidence for pluvial Lake Carrizo, San Luis Obispo County, California. In *From Saline to Freshwater: The Diversity of Western Lakes in Space and Time*; Starratt, S.T., Rosen, M.R., Eds.; Geological Society of America: Boulder, CO, USA, 2021; Volume 536, pp. 289–317.
37. Stephenson, R.K. Lithostratigraphic Record of North Soda Lake, Carrizo Plain, San Luis Obispo County, California: Implications for Late Pleistocene Paleoclimate in a Closed Hypersaline Lake Basin. Master's Thesis, California State University of Bakersfield, Bakersfield, CA, USA, 2013.
38. Eigenbrode, J.L. Sedimentological, Carbon-Isotopic, and Molecular Records of Late Holocene Climate in the Sediments of Soda Lake, Carrizo Plain, California. Master's Thesis, Indiana University, Bloomington, IN, USA, 1999.
39. Hill, M.L.; Dibblee, T.W. San Andreas, Garlock, and Big Pine faults, California: A study of the character, history, and tectonic significance of their displacements. *Geol. Soc. Am. Bull.* **1953**, *64*, 443–458. [[CrossRef](#)]
40. Dibblee, T.W. Displacements on the San Andreas rift zone and related structures in Carrizo Plain and vicinity. In *Guidebook: Geology of Carrizo Plains and San Andreas Fault*; Hackell, O., Dibblee, T.W., Jr., Hudson, F.S., White, G.H., Simonson, R.R., Fletcher, G.L., Wells, R.J., Graff, L.B., Hall, C.A., Jr., Christiensen, E.W., Eds.; San Joaquin Geological Society: Bakersfield, CA, USA; Pacific Section, AAPG: Bakersfield, CA, USA; SEPM: Tulsa, OK, USA, 1962; pp. 5–12.
41. Crowell, J.C. *San Andreas Fault in Southern California: A Guide to San Andreas Fault from Mexico to Carrizo Plain*; Division of Mines and Geology: Sacramento, CA, USA, 1975; 272p.
42. Galehouse, J.S. Provenance and Paleocurrents of the Paso Robles Formation, California. *Geol. Soc. Am. Bull.* **1967**, *78*, 951–958. [[CrossRef](#)]
43. Rosen, M.R. The importance of groundwater in playas: A review of playa classifications and the sedimentology and hydrology of playas. In *Paleoclimate and Basin Evolution of Playa Systems*; Rosen, M., Ed.; Geology Society of America: Boulder, CO, USA, 1994; Volume 289, pp. 1–18.
44. Rodriguez, A. Paleoenvironmental Study Based on North Soda Lake Sediments, San Luis Obispo County, California: Results of Mineralogical, Grain Size, and Geochemical Analyses. Master's Thesis, California State University of Bakersfield, Bakersfield, CA, USA, 2020.
45. Watanabe, M. Sample preparation for X-ray fluorescence analysis IV. Fusion bead method—Part 1 basic principals. *Rigaku J.* **2015**, *12*, 12–17.
46. Henderson, P. General geochemical properties and abundances of the rare earth elements. In *Developments in Geochemistry*; Henderson, P., Ed.; Department of Mineralogy, British Museum (Natural History): London, UK, 1984; Volume 2, pp. 1–32.
47. Boynton, W.V. Cosmochemistry of the rare earth elements: Meteorite Studies. In *Developments in Geochemistry*; Henderson, P., Ed.; Department of Mineralogy, British Museum (Natural History): London, UK, 1984; Volume 2, pp. 63–114.
48. Pettijohn, F.J.; Potter, P.E.; Siever, R. *Sand and Sandstone*; Springer: New York, NY, USA, 1987; 553p.
49. Herron, M.M. Geochemical Classification of Terrigenous Sands and Shales from Core or Log Data. *J. Sediment. Res.* **1988**, *58*, 820–829.
50. Fedo, C.M.; Nesbitt, H.W.; Young, G.M. Unraveling the effects of K metasomatism in sedimentary rocks and paleosols with implications for paleo-weathering conditions and provenance. *Geology* **1995**, *23*, 921–924. [[CrossRef](#)]

51. Nesbitt, H.W.; Young, G.M. Early Proterozoic Climates and Plate Motions Inferred from Major Element Chemistry of Lutites. *Nature* **1982**, *299*, 715–717. [[CrossRef](#)]
52. McLennan, S.M.; Hemming, S.; McDaniel, D.K.; Hanson, G.N. Geochemical approaches to sedimentation, provenance, and tectonics. In *Processes Controlling the Composition of Clastic Sediments*; Johnsson, M.J., Basu, A., Eds.; Geological Society of America: Boulder, CO, USA, 1993; Volume 284, pp. 21–40.
53. Jeong, G.Y.; Choi, J.H.; Lim, H.S.; Seong, C.; Yi, S.B. Deposition and weathering of Asian dust in Paleolithic sites, Korea. *Quat. Sci. Rev.* **2013**, *78*, 283–300. [[CrossRef](#)]
54. Chang, H.; An, Z.S.; Wu, F.; Jin, Z.D.; Liu, W.G.; Song, Y.G. A Rb/Sr record of the weathering response to environmental changes in westerly winds across the Tarim Basin in the late Miocene to the early Pleistocene. *Palaeogeogr. Palaeoclimatol. Palaeoecol.* **2013**, *386*, 364–373. [[CrossRef](#)]
55. Zou, C.; Mao, L.; Tan, Z.; Zhou, L.; Liu, L. Geochemistry of major and trace elements in sediments from the Lubei Plain, China: Constraints for paleoclimate, paleosalinity, and paleoredox environment. *J. Asian Earth Sci.* **2021**, *6*, 100071. [[CrossRef](#)]
56. Lerman, A. *Lakes: Chemistry, Geology, Physics*; Springer Press: Berlin/Heidelberg, Germany, 1978; 366p.
57. Meng, Q.T.; Liu, Z.J.; Bruch, A.A.; Liu, R.; Hu, F. Palaeoclimatic evolution during Eocene and its influence on oil shale mineralization, Fushun basin, China. *J. Asian Earth Sci.* **2012**, *45*, 95–105. [[CrossRef](#)]
58. Cao, H.S.; Guo, W.; Shan, X.L.; Ma, L.; Sun, P.C. Paleolimnological environments and organic accumulation of the Nenjiang Formation in the southeastern Songliao Basin, China. *Oil Shale* **2015**, *32*, 5–24. [[CrossRef](#)]
59. Wang, Z.W.; Wang, J.; Fu, X.G.; Zhan, W.Z.; Armstrong-Altrin, J.S.; Yu, F.; Feng, X.L.; Song, C.Y.; Zeng, S.Q. Geochemistry of the Upper Triassic black mudstones in the Qiangtang Basin, Tibet: Implications for paleoenvironment, provenance, and tectonic setting. *J. Asian Earth Sci.* **2018**, *160*, 118–135. [[CrossRef](#)]
60. Wang, Z.W.; Yu, F.; Wang, J.; Fu, X.G.; Chen, W.B.; Zeng, S.Q.; Song, C.Y. Palaeoenvironment evolution and organic matter accumulation of the Upper Triassic mudstones from the eastern Qiangtang Basin (Tibet), eastern Tethys. *Mar. Pet. Geol.* **2021**, *130*, 105133. [[CrossRef](#)]
61. Janz, T.; Vennemann, T.W. Isotopic composition (O, C, Sr, and Nd) and trace element ratios (Sr/Ca, Mg/Ca) of Miocene marine and brackish ostracods from North Alpine foreland deposits (Germany and Austria) as indicators for paleoclimate. *Palaeogeogr. Palaeoclimatol. Palaeoecol.* **2005**, *255*, 216–247. [[CrossRef](#)]
62. Wang, Z.W.; Fu, X.G.; Feng, X.L.; Song, C.Y.; Wang, D.; Chen, W.B.; Zeng, S.Q. Geochemical features of the black shales from the Wuyu Basin, southern Tibet: Implications for palaeoenvironment and palaeoclimate. *Geol. J.* **2017**, *52*, 282–297. [[CrossRef](#)]
63. Zhang, S.H.; Liu, C.Y.; Liang, H.; Wang, J.Q.; Bai, J.K.; Yang, M.H.; Liu, G.H.; Huang, H.X.; Guan, Y.C. Paleoenvironmental conditions, organic matter accumulation, and unconventional hydrocarbon potential for the Permian Lucaogou Formation organic-rich rocks in Santanghu Basin, NW China. *Int. J. Coal Geol.* **2018**, *185*, 44–60. [[CrossRef](#)]
64. Cao, J.; Wu, M.; Chen, Y.; Hu, K.; Bian, L.Z.; Wang, L.G.; Zhang, Y. Trace and rare earth element geochemistry of Jurassic mudstones in the northern Qaidam Basin, northwest China. *Geochemistry* **2012**, *72*, 245–252. [[CrossRef](#)]
65. Shen, J.; Schoepfer, S.D.; Feng, Q.L.; Zhou, L.; Yu, J.X.; Song, H.Y.; Wei, H.Y.; Algeo, T.J. Marine productivity changes during the end-Permian crisis and Early Triassic recovery. *Earth Sci. Rev.* **2015**, *149*, 136–162. [[CrossRef](#)]
66. Algeo, T.J.; Henderson, C.M.; Tong, J.N.; Feng, Q.L.; Yin, H.F.; Tyson, R.V. Plankton and productivity during the Permian-Triassic boundary crisis: An analysis of organic carbon fluxes. *Glob. Planet. Change* **2013**, *105*, 52–67. [[CrossRef](#)]
67. Schoepfer, S.D.; Shen, J.; Wei, H.Y.; Tyson, R.V.; Ingall, E.; Algeo, T.J. Total organic carbon, organic phosphorus, and biogenic barium fluxes as proxies for paleomarine productivity. *Earth Sci. Rev.* **2015**, *149*, 23–52. [[CrossRef](#)]
68. Dymond, J.; Suess, E.; Lyle, M. Barium in Deep-Sea Sediment: A Geochemical Proxy for Paleoproductivity. *Paleoceanography* **1992**, *7*, 163–181. [[CrossRef](#)]
69. Jones, B.F.; Bowser, C.J. The mineralogy and related chemistry of lake sediments. In *Lakes—Chemistry, Geology, Physics*; Lerman, A., Ed.; Springer: New York, NY, USA, 1978; pp. 179–235.
70. Davison, W. Iron and manganese in lakes. *Earth-Sci. Rev.* **1993**, *34*, 119–163. [[CrossRef](#)]
71. Jones, B.; Manning, D.A.C. Comparison of geochemical indices used for the interpretation of palaeoredox conditions in ancient mudstones. *Chem. Geol.* **1994**, *111*, 111–129. [[CrossRef](#)]
72. Arthur, M.A.; Sageman, B.B. Marine black shales: Depositional mechanisms and environments of ancient deposits. *Annu. Rev. Earth Planet. Sci.* **1994**, *22*, 499–551. [[CrossRef](#)]
73. Pattan, J.N.; Masuzawa, T.; Borole, D.V.; Parthiban, G.; Jauhari, P.; Yamamoto, M. Biological productivity, terrigenous influence and noncrustal elements supply to the Central Indian Ocean Basin: Paleoceanography during the past ~ 1 Ma. *J. Earth Syst. Sci.* **2005**, *114*, 63–74. [[CrossRef](#)]
74. Rollinson, H.R. *Using Geochemical Data: Evaluation, Presentation, Interpretation*; Routledge: Abingdon, UK, 1993; 384p.
75. Tanaka, K.; Akagawa, F.; Yamamoto, K.; Tani, Y.; Kawabe, I.; Kawai, T. Rare earth element geochemistry of Lake Baikal sediment: Its implication for geochemical response to climate change during the Last Glacial/Interglacial transition. *Quat. Sci. Rev.* **2007**, *26*, 1362–1368. [[CrossRef](#)]
76. Cullers, R.; Chaudhuri, S.; Kilbane, N.; Koch, R. Rare-earths in size fractions and sedimentary rocks of Pennsylvanian-Permian age from the mid-continent of the U.S.A. *Geochim. Cosmochim. Acta* **1979**, *43*, 1285–1301. [[CrossRef](#)]
77. Condie, K.C. Another look at rare earth elements in shales. *Geochim. Cosmochim. Acta* **1991**, *55*, 2527–2531. [[CrossRef](#)]

78. McLennan, S.M.; Taylor, S.R. Sedimentary rocks and crustal evolution: Tectonic setting and secular trends. *J. Geol.* **1991**, *99*, 1–21. [[CrossRef](#)]
79. Garzanti, E.; Resentini, A. Provenance control on chemical indices of weathering (Taiwan river sands). *Sed. Geol.* **2016**, *336*, 81–95. [[CrossRef](#)]
80. Dinis, P.A.; Garzanti, E.; Hahn, A.; Vermeesch, P.; Cabral-Pinto, M. Weathering indices as climate proxies. A step forward based on Congo and SW African river muds. *Earth-Sci. Rev.* **2020**, *201*, 103039. [[CrossRef](#)]
81. Pye, K.; Krinsley, D.H. Diagenetic carbonate and evaporite minerals in Rotliegend aeolian sandstones of the southern North Sea: Their nature and relationship to secondary porosity. *Clay Miner.* **1986**, *21*, 443–457. [[CrossRef](#)]
82. Werne, J.P.; Sageman, B.B.; Lyons, T.; Hollander, D.J. An integrated assessment of a “type euxinic” deposit: Evidence for multiple controls on black shale deposition in the Middle Devonian Oatka Creek Formation. *Am. J. Sci.* **2002**, *302*, 110–143. [[CrossRef](#)]
83. Haug, G.H.; Gunther, D.; Peterson, L.C.; Sigman, D.M.; Hughen, K.A.; Aeschlimann, B. Climate and the collapse of Maya civilization. *Science* **2003**, *299*, 1731–1735. [[CrossRef](#)] [[PubMed](#)]
84. Roy, P.D.; Caballero, M.; Lozano, R.; Ortega, B.; Lozano, S.; Pi, T.; Israde, I.; Morton, O. Geochemical record of Late Quaternary paleoclimate from lacustrine sediments of paleo-lake San Felipe, western Sonora Desert, Mexico. *J. S. Am. Earth Sci.* **2010**, *29*, 586–596. [[CrossRef](#)]
85. Andersson, P.O.D.; Worden, R.H.; Hodgson, D.M.; Flint, S. Provenance evolution and chemostratigraphy of a Paleozoic submarine fan-complex: Tanqua Karoo Basin, South Africa. *Mar. Petrol. Geol.* **2004**, *21*, 555–577. [[CrossRef](#)]
86. Chen, J.; Wang, Y.J.; Ji, J.F.; Lu, H.Y. The Rb/Sr value of the Luochuan loess section in Shaanxi and its climatic stratigraphic significance. *Quat. Sci.* **1999**, *4*, 350–356. (In Chinese)
87. Huang, R.; Zhu, C.; Zheng, C.G.; Ma, C.M. The distribution characteristics of Rb and Sr in the strata of the Zhongba site in the Three Gorges of the Yangtze River and its paleoclimate evolution. *Quat. Sci.* **2004**, *5*, 53–58. (In Chinese)
88. Pang, J.L.; Huang, C.C.; Zhang, Z.P. Rb and Sr composition of loess profile in Qishan, Shaanxi and high-resolution climate change. *Acta Sedimentol. Sin.* **2001**, *19*, 637–641. (In Chinese)
89. Shen, H.Y.; Jia, Y.L.; Li, X.S.; Wu, J.L.; Wei, L.; Wang, P.L. The composition of Rb, Sr and environmental changes of lake sediments of different sizes in Huangqihai, Inner Mongolia. *Acta Geogr. Sin.* **2006**, *61*, 1208–1217. (In Chinese)
90. Izumida, H.; Yoshimura, T.; Suzuki, A.; Nakashima, R.; Ishimura, T.; Yasuhara, M.; Inamura, A.; Shikazono, N.; Kawahata, H. Biological and water chemistry controls on Sr/Ca, Ba/Ca, Mg/Ca, and $\delta^{18}\text{O}$ profiles in freshwater pearl mussel *Hyriopsis* sp. *Palaeogeogr. Palaeoclimatol. Palaeoecol.* **2011**, *309*, 298–308. [[CrossRef](#)]
91. Poulain, C.; Gillikin, D.P.; Thébaud, J.; Munaron, J.M.; Bohn, M.; Robert, R.; Paulet, Y.-M.; Lorrain, A. An evaluation of Mg/Ca, Sr/Ca, and Ba/Ca ratios as environmental proxies in aragonite bivalve shells. *Chem. Geol.* **2015**, *396*, 42–50. [[CrossRef](#)]
92. Tyrrell, T. The relative influences of nitrogen and phosphorus on oceanic primary production. *Nature* **1999**, *400*, 525–531. [[CrossRef](#)]
93. Benitez-Nelson, C.R. The biogeochemical cycling of phosphorus in marine systems. *Earth Sci. Rev.* **2000**, *51*, 109–135. [[CrossRef](#)]
94. Dymond, J.; Collier, R. Particulate barium fluxes and their relationships to biological productivity. *Deep Sea Res. Part II* **1996**, *43*, 1283–1308. [[CrossRef](#)]
95. Pyle, K.M.; Hendry, K.R.; Sherrell, R.M.; Meredith, M.P.; Venables, H.; Lagerström, M.; Morte-Rodenas, A. Coastal barium cycling at the West Antarctic Peninsula. *Deep Sea Res. Part II* **2017**, *139*, 120–131. [[CrossRef](#)]
96. Dean, W.E.; Gardner, J.V.; Piper, D.Z. Inorganic geochemical indicators of glacial-interglacial changes in productivity and anoxia on the California continental margin. *Geochem. Cosmochim. Acta* **1997**, *61*, 4507–4518. [[CrossRef](#)]
97. Qadrouh, A.N.; Alajmi, M.S.; Alotaibi, A.M.; Baioumy, H.; Almalki, M.A.; Alyousif, M.M.; Salim, A.M.A.; Bin Rogaib, A.M. Mineralogical and geochemical imprints to determine the provenance, depositional environment, and tectonic setting of the Early Silurian source rock of the Qusaiba shale, Saudi Arabia. *Mar. Petrol. Geol.* **2021**, *130*, 105131. [[CrossRef](#)]
98. Hatch, J.R.; Leventhal, J.S. Relationship between inferred redox potential of the depositional environment and geochemistry of the Upper Pennsylvanian (Missourian) Stark shale member of the Dennis limestone, Wabaunsee country, Kansas, USA. *Chem. Geol.* **1992**, *99*, 65–82. [[CrossRef](#)]
99. Tribouillard, N.; Algeo, T.J.; Lyons, T.; Riboulleau, A. Trace metals as paleoredox and paleoproductivity proxies: An update. *Chem. Geol.* **2006**, *232*, 12–32. [[CrossRef](#)]
100. Heusser, L.E.; Kirby, M.E.; Nichols, J.E. Pollen-based evidence of extreme drought during the last Glacial (32.6–9.0 ka) in coastal southern California. *J. Quat. Sci.* **2015**, *26*, 243–253. [[CrossRef](#)]
101. Clark, P.U.; Shakun, J.D.; Baker, P.A.; Williams, J.W. Global climate evolution during the last deglaciation. *Proc. Natl. Acad. Sci. USA* **2012**, *109*, E1134–E1142. [[CrossRef](#)]
102. Enzel, Y.; Wells, S.G.; Lancaster, N. Late Pleistocene lakes along the Mojave River, southwest California. In *Paleoenvironments and Paleohydrology of the Mojave and Southern Great Basin Deserts*; Enzel, Y., Wells, S.G., Lancaster, N., Eds.; Geological Society of America: Boulder, CO, USA, 2003; Volume 368, pp. 61–77.
103. Kindler, P.; Guillevic, M.; Baumgartner, M.; Schwander, J.; Landais, A.; Leuenberger, M. Temperature reconstruction from 10 to 120 kyr b2k from the NGRIP ice core. *Clim. Past* **2014**, *10*, 887–902. [[CrossRef](#)]
104. Seki, O.; Ishiwatari, R.; Matsumoto, K. Millennial climate oscillations in NE Pacific surface waters over the past 82,000 years: Fresh insights from alkenones. *Geophys. Res. Lett.* **2002**, *29*, 2144. [[CrossRef](#)]

105. Svensson, A.; Andersen, K.K.; Bigler, M.; Clausen, H.B.; Dahl-Jensen, D.; Davies, S.M.; Johnsen, S.J.; Muscheler, R.; Parrenin, F.; Rasmussen, S.O.; et al. A 60,000-year Greenland stratigraphic ice core chronology. *Clim. Past* **2008**, *4*, 47–57. [[CrossRef](#)]
106. Barron, J.A.; Bukry, D.; Field, D.B.; Finney, B. Response of diatoms and silicoflagellates to climate change and warming in the California Current during the past 250 years and the recent rise of the toxic diatom *Pseudo-nitzschia australis*. *Quat. Int.* **2013**, *310*, 140–154. [[CrossRef](#)]
107. McGann, M. Late Quaternary pollen record from the central California continental margin. *Quat. Int.* **2015**, *387*, 46–57. [[CrossRef](#)]

Disclaimer/Publisher’s Note: The statements, opinions and data contained in all publications are solely those of the individual author(s) and contributor(s) and not of MDPI and/or the editor(s). MDPI and/or the editor(s) disclaim responsibility for any injury to people or property resulting from any ideas, methods, instructions or products referred to in the content.